THE JOURNAL OF BIOLOGICAL CHEMISTRY VOL. 289, NO. 12, pp. 8588–8598, March 21, 2014

A Novel Structural Unit in the N-terminal Region of Filamins*[S]

Received for publication, November 25, 2013, and in revised form, January 21, 2014 Published, JBC Papers in Press, January 27, 2014, DOI 10.1074/jbc.M113.537456

Ritika Sethi[‡1], Jonne Seppälä[‡], Helena Tossavainen[§], Mikko Ylilauri[‡], Salla Ruskamo[¶], Olli T. Pentikäinen[‡], Ulla Pentikäinen[‡], Perttu Permi[§], and Jari Ylänne[‡2]

From the [‡]Department of Biological and Environmental Science and Nanoscience Center, University of Jyväskylä, P. O. Box 35, Survontie 9, 40014 Jyväskylä, the [§]Program in Structural Biology and Biophysics, Institute of Biotechnology, University of Helsinki, FI-00014 Helsinki, and the [¶]Department of Biochemistry and Biocenter Oulu, University of Oulu, P. O. Box 3000, 90014 Oulu, Finland

Background: Filamins are actin cross-linking and signaling scaffolding proteins where C-terminal domains have inter-domain interactions but little is known about the N-terminal domains.
Results: Crystal structures of N-terminal domains 3–5 reveal novel domain packing and interaction details of domain 4.
Conclusion: Domain 4 is stabilized by interaction with domain 5.
Significance: Here, inter-domain interactions positively regulate domain 4 interactions with ligands.

Immunoglobulin-like (Ig) domains are a widely expanded superfamily that act as interaction motifs or as structural spacers in multidomain proteins. Vertebrate filamins (FLNs), which are multifunctional actin-binding proteins, consist of 24 Ig domains. We have recently discovered that in the C-terminal rod 2 region of FLN, Ig domains interact with each other forming functional domain pairs, where the interaction with signaling and transmembrane proteins is mechanically regulated by weak actomyosin contraction forces. Here, we investigated if there are similar inter-domain interactions around domain 4 in the N-terminal rod 1 region of FLN. Protein crystal structures revealed a new type of domain organization between domains 3, 4, and 5. In this module, domains 4 and 5 interact rather tightly, whereas domain 3 has a partially flexible interface with domain 4. NMR peptide titration experiments showed that within the three-domain module, domain 4 is capable for interaction with a peptide derived from platelet glycoprotein Ib. Crystal structures of FLN domains 4 and 5 in complex with the peptide revealed a typical β sheet augmentation interaction observed for many FLN ligands. Domain 5 was found to stabilize domain 4, and this could provide a mechanism for the regulation of domain 4 interactions.

Filamins (FLNs)[3] are homodimeric actin cross-linking proteins that are required for multicellular tissue differentiation. All three *FLN* genes (*FLNA*, *FLNB*, and *FLNC*) are essential in mouse and truncation or substitution mutations cause developmental defects in humans (1, 2) (Fig. 1). The diversity of phenotypes caused by *FLN* mutations can be explained by at least 90 proteins that interact with FLNs (3). The interaction partners can be classified to at least three different categories: transmembrane proteins, cytoskeletal proteins, and intracellular signaling proteins. Thus, FLNs are involved in stabilization and regulation of plasma membrane, regulation of actin cytoskeleton, and intracellular signaling (3–8).

Structurally, vertebrate FLNs consist of an N-terminal actin-binding domain and 24 immunoglobulin-like (Ig) domains (the dimer is shown in Fig. 1). Domains 1–15 are referred to as rod 1 and 16–24 as rod 2. The structure of the actin-binding domain is similar to that of α-actinin and is composed of two calponin homology domains (9, 10). The FLN Ig domains have a characteristic structure and they can be regarded as protein interaction modules. They often interact with other proteins by a β sheet augmentation mechanism. In this mechanism, the interaction partner forms an additional β-strand next to the strand C of the FLN domain and simultaneously interacts with the hydrophobic groove between the strands C and D, called the CD face (11–14). It is using this mode that ligands like transmembrane receptors of the integrin family (12, 15, 16), the platelet von Willebrand factor receptor subunit glycoprotein Ib (GPIb) (11), and the cystic fibrosis transmembrane conductance regulator (17, 18) interact with FLNa domains 17, 19, 21, and 23. Also, signaling protein FilGAP uses the same mechanism for interacting with FLNa domain 23 (4) and migfilin with FLNa domain 21 (13, 14). Biochemical studies have also suggested that FLNa domain 4 interacts in a similar way with many of the ligands (19). Interestingly, in the dimerization interface of FLNc and FLNa, domain 24 also utilizes the CD face, but the β sheet augmentation occurs through strand D (20, 21).

* This work was supported by grants from the Marie Curie Actions FP 7 grant to Initial Training Network MUZIC (Muscle Z-disk Protein Complexes: from atomic structure to physiological function) (to R. S. and J. Y.), the National Doctoral Programme in Informational and Structural Biology (to M. Y.), and Sigrid Juselius Foundation and Academy of Finland Grants 114713 and 138327 (to J. Y.) and 263794 and 259447 (to P. P.), and CSC-Finnish IT Center for Science computational Grants jyy2516 and jyy2586 (to O. T. P.).
[S] This article contains supplemental Figs. S1–S3.
The atomic coordinates and structure factors (codes 3V8O, 4M9P, and 4MGX) have been deposited in the Protein Data Bank (http://wwpdb.org/).
Chemical shifts for NMR assignments have been deposited to the BioMagResBank database under accession numbers 19496 (FLNa3–5) and 19495 (FLNc4–5).
[1] To whom correspondence may be addressed. Tel.: 358440777438; E-mail: ritika.sethi@jyu.fi.
[2] To whom correspondence may be addressed. Tel.: 358504285273; Fax +35814617 239; E-mail: jari.p.ylanne@jyu.fi.
[3] The abbreviations used are: FLN, filamin; GPIb, glycoprotein Ib; EOM, ensemble optimization method; MD, molecular dynamics; SAXS, small angle x-ray scattering; HSQC, heteronuclear single quantum coherence; PDB, Protein Data Bank.

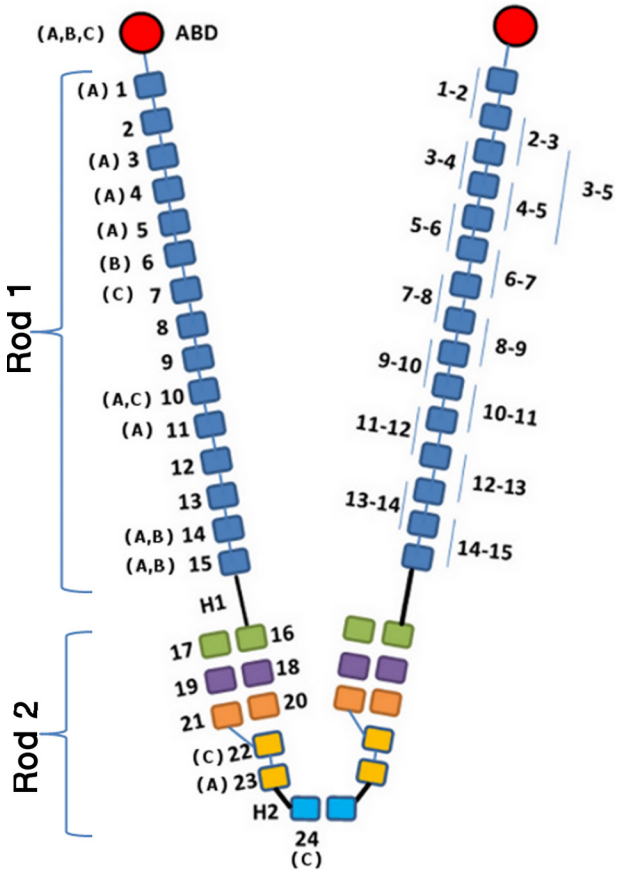

FIGURE 1. **Schematic representation of filamin dimer structure.** Actin-binding domains (*ABDs*) are *red*, followed by 24 Ig domains. Three known domain pairs in the rod 2 region (16–17, 18–19, and 20–21) are shown in *green*, *purple*, and *orange*, respectively. The fragments of the rod 1 region investigated in this study are labeled on the *right* subunit. Isoform-specific (*FLNA*, *FLNB*, and *FLNC*) substitution and local deletion mutations in human patients are shown on the *left* subunit.

There are three structurally characterized, closely interacting domain pairs in the C-terminal rod 2 region of FLNa: domains 16–17, 18–19, and 20–21 (15, 22). Interestingly, in FLNa domain pairs 18–19 and 20–21, the function of the even numbered domain is to mask the CD face of the odd domain (15, 22) and this masking can be relieved by (*a*) low pico-Newton range mechanical forces that lead to a tighter interaction between FLN domain and ligand (23–25); or (*b*) displacement of the even numbered domain by the ligand itself, albeit with a lower affinity (26, 27). To find out if similar structural mechanisms could regulate the interactions of FLN domain 4, we solved the crystal structures of FLNa domains 3–5, FLNc domains 4–5, and FLNc domains 4–5 in complex with GPIb peptide. These structures disclosed a completely new type of interaction between three Ig domains.

EXPERIMENTAL PROCEDURES

Protein Expression and Purification—Fragments of the human *FLNC* and *FLNA* cDNA (GenBank™ AJ012737 and AB593010.1) were PCR amplified according to the predicted domain boundaries (7) and cloned to the GST fusion protein vector pGTVL1 (Structural Genomics Consortium, University of Oxford) according to the ligation-independent cloning method (28). The final products were verified by DNA sequencing. The proteins were expressed in *Escherichia coli* BL21 Gold cells (Agilent Technologies) at 37 °C for 4 h with 0.4 mM isopropyl β-D-1-thiogalactopyranoside. The bacterial pellets were lysed using French press. The proteins were captured with glutathione-agarose column (Protino glutathione-agarose 4B, Macherey-Nagel), released with Tobacco Etch virus protease (Invitrogen), and further purified by size exclusion chromatography with a HiLoad 26/60 Superdex 75 column (GE Healthcare) in 100 mM NaCl, 1 mM dithiothreitol (DTT), 20 mM Tris, pH 7.5 (FLNc fragments), and 100 mM NaCl, 1 mM DTT, 20 mM Tris, pH 8.0 (FLNa fragments). Finally, the proteins were concentrated using Centriprep YM-10000 (Millipore). Mutants were generated using the QuikChange Multisite-directed mutagenesis kit (Agilent Technologies). $^{13}C/^{15}N$-Labeled FLNc4–5, FLNc5, and FLNa3–5 were expressed in *E. coli* in standard D-glucose/M9 minimal medium. These proteins were purified in 50 mM sodium phosphate, 100 mM NaCl, 1 mM DTT using the same protocol as described above for the unlabeled fragments.

Protein Crystallography—Crystallization trials with hanging drop vapor diffusion method were set up for the purified recombinant proteins at room temperature. First crystals for FLNc4–5 were obtained in 1.4 M sodium potassium phosphate. The condition was optimized using a gradient of salt concentration and the final crystals were mounted from 1.6 M sodium potassium phosphate. These were first cryo-protected by adding 30% glycerol (final concentration) to the mother liquor and then frozen in liquid nitrogen. The crystals for FLNa3–5 were obtained in 0.1 M sodium malonate, pH 4, 12% (w/v) polyethylene glycol (PEG) 3,350, and frozen in liquid nitrogen using 0.1 M sodium malonate, pH 4, 35% (w/v) polyethylene glycol 3,350. Equimolar mixture (1 mM each) of FLNc4–5 with GPIb peptide (residues 573–596, RGSLPTFRSSLFLWVRPNGRVGPL, numbering according to Uniprot ID P07359) was used to obtain co-crystals in 0.1 M HEPES, pH 7.5, 20% (w/v) PEG 8,000 using a 1:2 ratio of protein to mother liquor. The crystals were cryo-protected with 6.6% ethylene glycol and 16.6% glycerol.

The diffraction data were collected at 100 K at the ESRF beamline ID23-1 (wavelength = 1.07227 Å) (FLNc4–5) and ID29 (wavelength = 0.976250 Å) (FLNa3–5 and FLNc4–5/GPIb). The data were processed with XDS (29) and the structures were solved using molecular replacement with the program Phaser (30) using FLNc23 (PDB code 2NQC) chain A as the search model for FLNc4–5, FLNc4–5 (PDB code 3V8O), and FLNc23 (2D7Q) as models for FLNa3–5 structure, and FLNc4–5 (PDB code 3V8O) for the FLNc4–5/GPIb structure. Refinement and model building were performed by programs Refmac5 (31, 32) and Coot (33) for FLNc4–5 and FLNc4–5/GPIb. The model for FLNa3–5 was built using ARP/wARP 7.3 (34) and Coot and refined using Refmac5. The structure of FLNc4–5 was refined using medium noncrystallographic symmetry restraints between chains A and B. Structure factors and coordinates were deposited in the PDB with codes 3V8O (FLNc4–5), 4M9P (FLNa3–5), and 4MGX (FLNc4–5/GPIb). For FLNc4–5, 89.2% of amino acids were in the most favored region, 9.8% in additionally allowed regions, and 1% in generously allowed region of the Ramachandran plot. The values for FLNa3–5 were 92.1, 7.5, and 0.4%, respectively, and for FLNc4–5/GPIb, 77.6, 19.0, and 3.4%, respectively. Crystal

structure figures were generated using PyMOL (Schrödinger LLC, Portland, OR). The domain-domain interface was analyzed using the PISA server (35). Rendering was done in Chimera (36) according to the sequence alignment made with Clustal Omega (37) using FLNa/b/c3–5, FLNa3–5 of *Mus musculus, Gallus gallus, Danio rerio,* and *Drosophila melanogaster*.

Small Angle X-ray Scattering Measurements—Small angle x-ray scattering (SAXS) data were collected on the EMBL (European Molecular Biology Laboratory) X33 beamline at the DESY, Hamburg (38) (MAR345 image plate, sample-detector distance of 2.7 m and wavelength $\lambda = 0.15$ nm, covering the momentum transfer range $0.08 < s < 4.9\ nm^{-1}$ (where $s = 4\pi \sin(\theta)/\lambda$, 2θ = scattering angle)); MAX IV Laboratory, beamline Cassiopeia I911-SAXS at the MAX II storage ring (Lund, Sweden) (39) (PILATUS 1M image plate, sample-detector distance of 2.2 m and wavelength 0.091 nm, covering the momentum transfer range $0.1 < s < 3\ nm^{-1}$) and ESRF (European Synchrotron Radiation Facility), beamline BM29 (40) (PILATUS 1M image plate, sample-detector distance of 2.9 m and wavelength 0.10 nm, covering the momentum transfer range $0.01 < s < 5\ nm^{-1}$). The protein concentrations were in the range of 1–10 mg/ml in purification buffer supplemented with 10 mM DTT. Buffer subtractions were conducted with either BioXTAS RAW software (41) or ATSAS package program PRIMUS (42) and the scattering intensity (I) was extrapolated to zero solute concentration. The forward scattering $I(0)$ and the radius of gyration (R_g) were calculated using the program GUINIER (43), where at very small angles ($s \times R_g < 1.3$), the scattering intensity is the following.

$$I(s) = I(0)\exp(-1/3(R_g s)^2) \quad \text{(Eq. 1)}$$

The distance distribution functions $p(r)$ and the maximum particle dimensions D_{max} were calculated for all fragments using the program GNOM (44). The molecular mass of the constructs were evaluated by comparing the forward scattering with that from reference solution of bovine serum albumin (BSA) with molecular mass 66 kDa using Equation 2.

$$Mw_{sample} = I(0)_{sample} \times Mw_{ref}/I(0)_{ref} \quad \text{(Eq. 2)}$$

Assuming the samples are monodisperse, Porod's law was applied to find out the excluded volume of the hydrated particle as,

$$V = 2\pi^2 I(0) / \int_0^\infty s^2 I_{exp}(s) ds \quad \text{(Eq. 3)}$$

and to check the S^{-4} decay in scattering intensity at higher angles (45). Kratky plot (46) ($I(s) \times s^2$ *versus* s) was evaluated to check for the flexibility of the protein at higher scattering angles. The scattering patterns were further used to generate low resolution *ab initio* models of FLNc4–5 and FLNa3–5 by the programs DAMMIF (47) or GASBOR (48). Ten rounds of DAMMIF or GASBOR were done to generate models that were averaged using the program DAMAVER (49) to find the best model with common structural features. The scattering intensities of the crystal structures of FLNc4–5 (Protein Data Bank code 3V8O) and FLNa3–5 (PDB code 4M9P) were calculated using CRYSOL (50) and the superposition of the DAMAVER generated envelope with the respective crystal structures are done with the SUPCOMB program of the ATSAS package and the figures are made using PyMOL. To assess the flexibility of domain 3 in the FLNa and FLNc3–5 fragments, the ensemble optimization method (EOM) (51) was used. Similar analysis was performed for FLNc4–5 as an internal control. First, 10,000 randomized models (pool) were generated for each fragment using the native chain option in the RanCH program of the EOM package. The scattering profiles of each of these models were compared with the experimental scattering of the respective fragments (FLNa3–5, FLNc3–5, and FLNc4–5). A genetic algorithm was used to select a set of representative models (FLNa3–5 = 24; FLNc3–5 = 18, and FLNc4–5 = 12) from the pool such that the average scattering from the selected models fits the experimental scattering. The results were represented as R_g and D_{max} distribution profiles using GraphPad Prism version 4 for Windows (GraphPad Software Inc., La Jolla, CA).

Protein Interaction Assay—Pull-down assays were performed using GST-tagged FLNc4 bound to glutathione-agarose resin. 1–20 μM FLNc5 and FLNc5R755D was allowed to interact for 1 h at 23 °C after which the resin was washed three times with 500 μl of PBS, 1 mM DTT and eluted with 10 μl of the SDS-PAGE sample buffer. Proteins were fractionated by SDS-PAGE and visualized with Coomassie stain. Intensities of the protein bands were quantified by ImageJ (52). Data were plotted using GraphPad Prism version 5 for Windows to produce a non-linear regression curve for one site total and nonspecific binding (specific = $B_{max} \times X/(X + K_d)$; nonspecific = NS $\times$ X + background, where X = ligand concentration).

ThermoFluor Assay—Thermal stability of FLNc4, FLNc5, and FLNc4–5 was determined using Bio-Rad C1000 thermal cycler, CFx96 Real-Time system. Unfolding of the proteins was monitored using the fluorescent dye SYPRO Orange (Invitrogen), which binds to the hydrophobic core of the protein as it unfolds. A temperature gradient was set up from 20 to 95 °C with 0.5 °C/30-s increments. Each sample contained 100 μM protein, except FLNc4 (150 μM), and 5× dye in 25 μl total volume.

NMR Experiments—NMR samples were prepared in 50 mM NaH_2PO_4, 100 mM NaCl, 1 mM DTT buffer at pH 7.0. D_2O was added to obtain ~8% solutions. Protein concentrations were 0.4–1.2 mM. Measurement temperatures were 28 °C for FLNc5 and FLNc4–5, and 35 °C for FLNa3–5. For the chemical shift assignment HNCACB and CBCA(CO)NH spectra were recorded with a Varian INOVA 500 MHz spectrometer equipped with a ^{15}N,^{13}C,^{1}H triple-resonance z-PFG probehead for FLNc5 and a Varian INOVA 800 MHz spectrometer equipped with a cryogenically cooled, ^{15}N,^{13}C,^{1}H triple-resonance z-PFG probehead for FLNc4–5 and FLNa3–5. For FLNc4–5, the backbone amide assignment percentage was 95, whereas for FLNc5 all backbone amides were assigned. Peptide binding assays were performed by stepwise addition of the model peptide resulting in approximate concentration ratios of 1 (protein):0 (peptide), 1:0.5, 1:1, 1:2, 1:3, and 1:5. At each step a ^{1}H,^{15}N-heteronuclear single quantum coherence (HSQC) spectrum for the detection of backbone amide group chemical shift changes, and a ^{1}H,^{13}C-HSQC spectrum for the detection

of methyl group chemical shift changes in the case of FLNa3–5 was recorded. Chemical shift changes were calculated as $\Delta\delta = ((\Delta\delta_H)^2 + (0.15 \times \Delta\delta_N)^2)^{1/2}$. All spectra were processed with Vnmr 6.1C (Varian Inc.) and analyzed with Sparky 3.110 (T. D. Goddard and D. G. Kneller, University of California, San Francisco).

Molecular Dynamics Calculations—The x-ray structure of FLNa3–5 (PDB code 4M9P) was used as the starting structure for MD simulations. Before energy minimizations and MD simulations, TIP3P water molecules extending 13 Å in all dimensions around the solute and counter ions to obtain neutrality were added with LEAP (53). All energy minimizations and MD simulations were performed with NAMD 2.9 (54) using ff03 force field parameters (55). Before MD simulations, the system was relaxed and equilibrated. First the water molecules and counter ions were minimized using the steepest descent algorithm (3000 steps) keeping the rest of the system fixed. This was followed by similar minimization but only Cα-atoms were restrained to their crystallographic positions with a harmonic force of 5 kcal mol^{-2} Å^{-1}, whereas the rest of the system moved freely. Before starting the production of MD simulations, the equilibrium MD simulations for the whole system with Cα-atoms restrained were performed first at constant volume (for 300 ps) and then at constant pressure (for further 300 ps). Finally the whole system was equilibrated by simulating it at constant pressure without any restrains for 450 ps. After the system was fully equilibrated, the 50-ns production simulation was performed without constraints. Five parallel simulations were performed. During the simulations, the system was kept at constant temperature (300 K) using Langevin damping coefficient of 5 ps^{-1} and constant pressure (1 atm) using a Nosé-Hoover Langevin piston (56) with an oscillation timescale of 200 fs and damping time scale of 100 fs. 2-fs integration time steps were used under a multiple time stepping scheme (57), where bonded and short-range interactions were computed every time step and long-range electrostatic interactions every third time step. A cutoff of 12 Å for van der Waals and short-range electrostatic interactions was used. To ensure a smooth cutoff for van der Waals interactions, a switching function was started at 10 Å. Long-range electrostatic interactions were calculated using the particle-mesh Ewald method (58). Periodic boundary conditions were used in all simulations. The SHAKE algorithm was applied to constrain the bonds containing hydrogen atoms (59). Snapshots from trajectories obtained from MD simulation were extracted with PTRAJ in ANTECHAMBER (53).

RESULTS

Crystal Structures of FLNa Domains 3–5 and FLNc Domains 4–5 Show a Novel Domain-Domain Organization—The crystal structures of FLNa domains 3–5 (Fig. 2*A* and Table 1) and FLNc domains 4–5 (Fig. 2*B* and Table 1) disclosed a completely new type of interaction between three Ig domains (Fig. 2*A*) where the interfaces are highly conserved (Fig. 3 and supplemental Fig. S1). The domains interact side by side with each other along their β sheets. This leads to a sandwich structure where the β sheets of each domain stack roughly parallel on top of each other (Fig. 2*A*, *left side*), with domain 3 slightly shifted (Fig. 2*A*, *right side*). In this arrangement, the interaction between domains 3 and 4 is mediated via the edges of the β sheets, whereas domains 4 and 5 interact along three β-strands from each side. The buried interface area is about 500 and 830 Å^2 for domains 3–4 and 4–5, respectively, suggesting that the interaction between 4 and 5 is tighter than the other. There is a large hydrophobic interaction surface between domains 4 and 5 around a Trp residue in the A strand of domain 4 (Trp-582 in FLNa and Trp-577 in FLNc) (Fig. 2*C*), whereas the interaction between domains 3 and 4 has mostly polar characteristics. The main chain structure of FLNc domains 4–5 is largely identical to FLNa domains (root mean square deviation of 0.66 Å between 165 C-α atoms) (Fig. 2*B*).

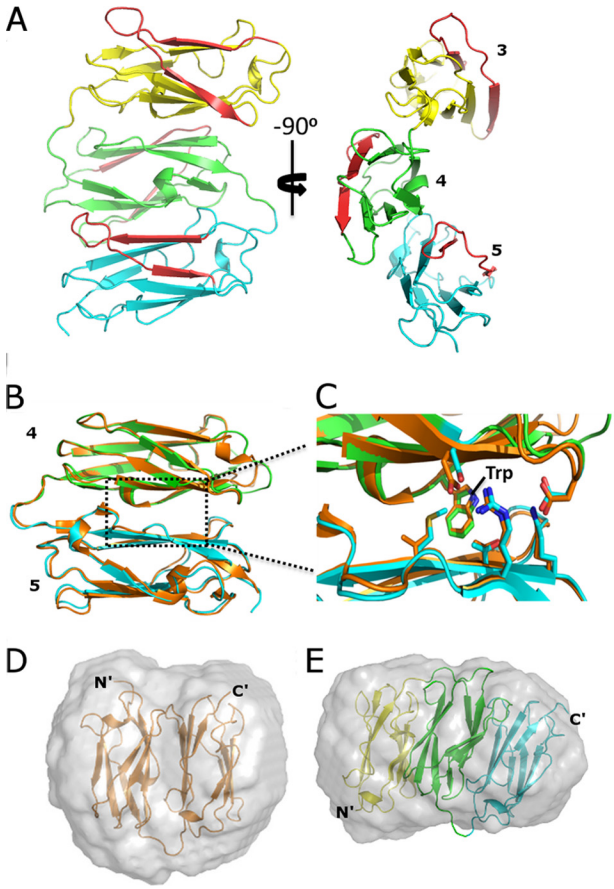

FIGURE 2. **New domain packing in FLNs.** *A*, two views of the crystal structure of FLNa3–5, where domains 3, 4, and 5 are shown in *yellow*, *green*, and *cyan*, respectively. β-Strands C and D are shown in *red*. *B*, superposition of FLNc4–5 (*orange*) with FLNa4–5 (domain coloring as in *panel A*). *C*, zoom-in view of the interface showing key residues. *D* and *E*, superposition of the FLNc4–5 and FLNa3–5 structures with their respective *ab initio* SAXS envelopes. Normalized spatial discrepancy of superposition for FLNc4–5 is 2.41 and FLNa3–5 is 1.63.

The domain-domain interactions observed in these crystal structures are, to our knowledge, unique among the entire Ig superfamily. Therefore, we used several complementary techniques to confirm that the domain arrangement and interactions exist also in solution and are not induced by crystal packing. First, we compared the crystal structures with the SAXS scattering data obtained in solution. The χ values for comparison of calculated scattering from the structures and observed solution scattering profile were 1.13 and 1.80 for FLNa domains

TABLE 1
Crystallography data collection and refinement statistics

	FLNc4–5 (PDB code 3V8O)	FLNa3–5 (PDB code 4M9P)	FLNc4–5/GPIb (PDB code 4MGX)
Data collection			
Space group	$P\ 2_12_12_1$	$P6_5$	$P4_322$
Cell dimensions			
a, *b*, *c*, Å	63.62, 91.35, 103.72	63.04, 63.04, 136.60	111.80, 111.80, 59.88
α, β, γ, degree	90, 90, 90	90, 90, 120	90, 90, 90
Resolution range, Å	46.63–2.8 (2.87–2.8)[a]	42.65–1.72 (1.76–1.72)	47.73–3.16 (3.24–3.16)
R_{sym}[b] (%)	15.8 (76.3)	9.7 (67.9)	20.5 (242.7)
$I/\sigma I$	9.92 (2.7)	18.24 (3.3)	9.53 (0.7)
Completeness, %	100 (98)	99.7 (96.5)	98.2 (100)
Redundancy	4.2 (4.2)	10.9 (8.0)	10.42 (7.8)
Refinement			
Resolution (Å)	46.63–2.8 (2.87–2.8)	42.65–1.72 (1.76–1.72)	47.73–3.16 (3.24–3.16)
No. of reflections			
Refinement	13602 (1012)	30839 (1623)	6556 (456)
Test set	1512 (113)	2204 (115)	345 (24)
R_{work}/R_{free} (%)	20/25.5 (33.4/40.1)	19.9/24.3 (24.5/30.6)	22.6/27.7 (35.9/45.6)
No. of atoms			
Protein	2854	2173	1439
Heterogen	1	Null	Null
Solvent	47	219	2
Root mean square differences			
Bond lengths (Å)	0.022	0.019	0.012
Bond angles, degree	1.8	1.98	1.80
Average B-factor, $Å^2$	29.3	22.18	108.48
Protein	29.28	21.95	108.48
Solvent	23.41	27.04	58.79

[a] Values of the last resolution shell in parentheses.
[b] Diederichs and Karplus (1997).

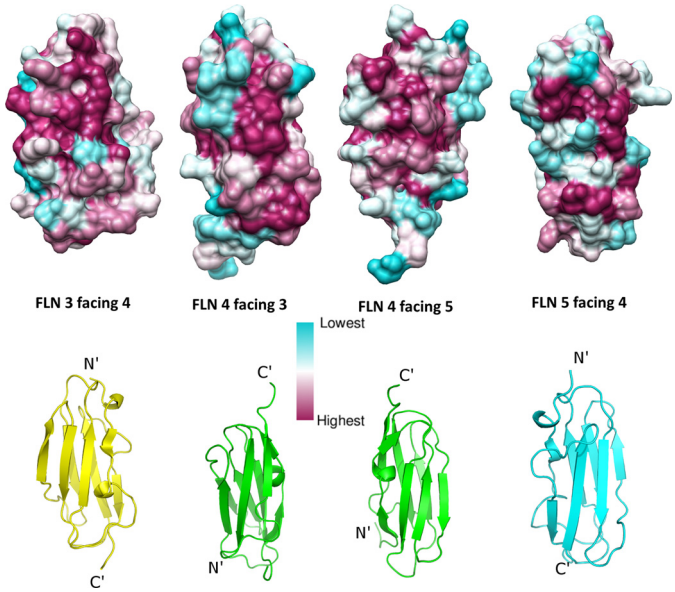

FIGURE 3. **Surface conservation of the domain-domain interfaces in FLN3–5.** Corresponding schematic models made using PyMOL are shown below the surface visualization. Sequence alignment is shown in supplemental Fig. S1.

TABLE 2
Parameters derived from SAXS measurements of FLN domains 4–5, mutants of FLNc4–5 and FLN 3–5

Protein	R_g[a]	~D_{max}[b]
	Nm	
FLN domains 4–5 constructs		
FLNc4–5	1.71 ± 0.01	4.8
FLNa4–5	1.90 ± 0.01	5.3
Mutation in FLNc4–5		
FLNc4 W577A	1.88 ± 0.01	6.5
FLNc4 D627R	1.85 ± 0.01	7.2
FLNc4 R755D	1.86 ± 0.01	6.7
FLNc4 W577A/D627R	1.85 ± 0.01	7.0
FLNc4 W577A/FLNc5R755D	2.04 ± 0.01	7.5
FLNc4D627R/FLNc5 R755D	1.85 ± 0.01	6.2
FLN domains 3–5 constructs		
FLNa 3–5	2.32[c]	7.7[c]
FLNc 3–5	2.41[c]	7.9[c]

[a] R_g, radius of gyration (mean square of the distances from the center of mass of the particle weighted by electron densities) from Equation 1.
[b] ~D_{max}, maximum dimension inside the particle estimated from distance distribution probability function. The values written here are with an approximate error of 0.5 nm.
[c] Average values reported using EOM.

3–5 and FLNc domains 4–5, respectively. The structures fitted well in the SAXS-generated *ab initio* envelopes (Fig. 2, *D* and *E*). Mutations of the contact residues seen in the crystal structure made the two-domain fragment FLNc4–5 more extended in SAXS (Table 2) and the same mutations also diminished the interaction between individual FLNc domains 4 and 5 in pull-down assays (Fig. 4, *A* and *B*). Comparison of NMR chemical shifts between FLNc domain 5 and the ins 4–5 pair also verified the interaction surface (Fig. 4, *C* and *D*, and supplemental Fig. S2).

In line with the relatively small interaction area between FLNa domains 3 and 4, closer analysis of SAXS data using EOM suggested that in both, FLNa and FLNc, three domain fragments of domains 3–5 can be flexible in solution. This is shown by the broader D_{max} range for three domain fragments as compared with FLNc4–5 (Fig. 5, *A* and *B*). To further test flexibility of the FLNa3–5 structure, we performed MD simulations on FLNa3–5 without any restraints. Analysis of the snapshot structures obtained from 50-ns MD simulations showed that domain 3 changes its orientations with respect to domains 4 and 5 whose interactions stay intact (Fig. 5*C*). This flexibility of the three-domain fragment observed in the MD simulations is in accordance with the observed solution scattering profile of FLNa3–5 (χ values for snapshots of two extreme orientations in the range of 1.15–1.23) and the snapshots fit well in the SAXS-generated *ab initio* envelopes (Fig. 5*D*).

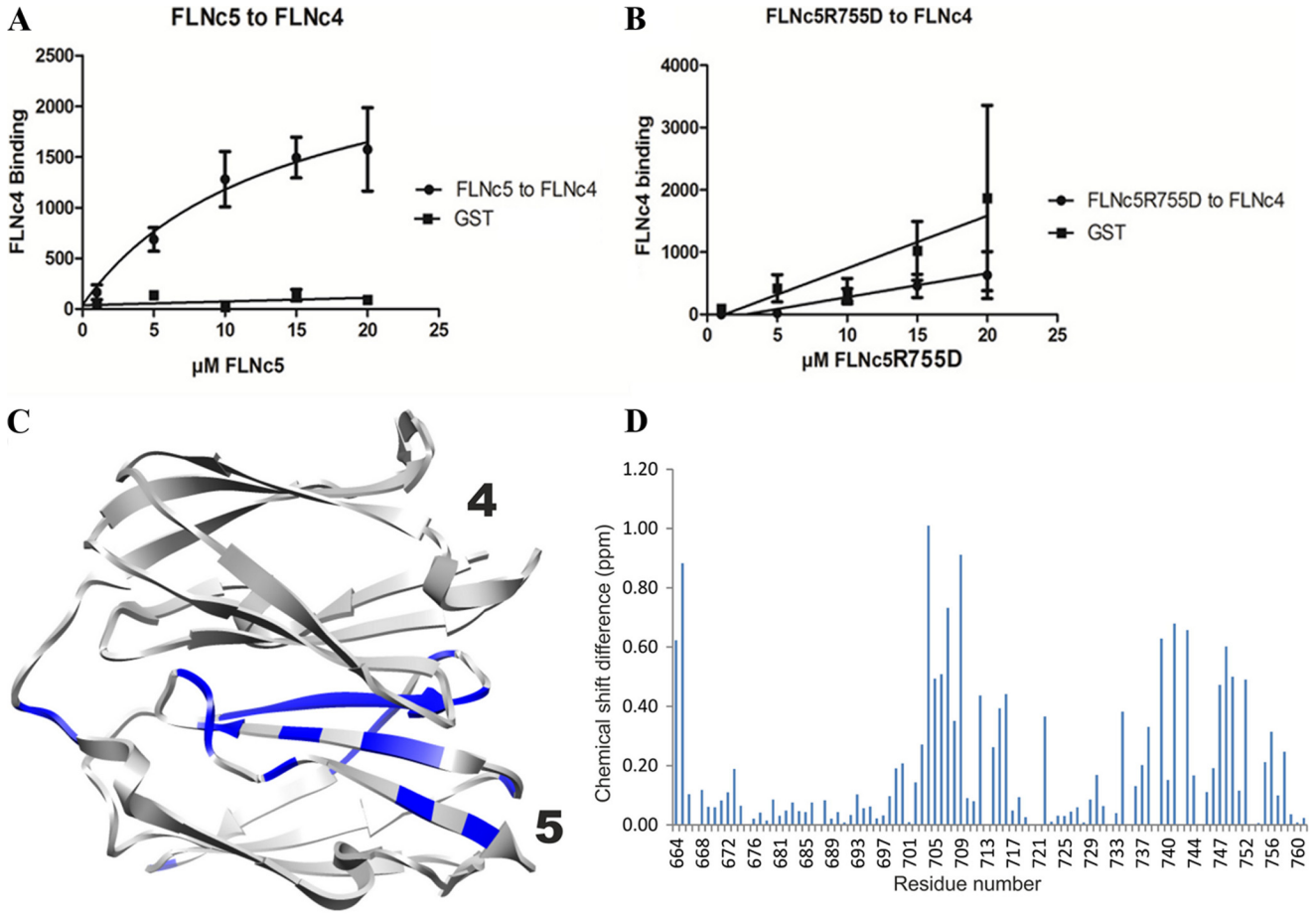

FIGURE 4. **Confirmation of the FLNc4–5 interface.** *A,* quantification of the binding observed from the pulldown assay of FLNc4 and FLNc5. *B,* plot obtained from the pulldown assay of FLNc4 and FLNc5R755D showing a decline in the interaction. *Bars* show S.E. between three independent experiments. *C,* structural representation of the NMR measurements showing residues in *blue* that have chemical shift differences of more than 0.25 ppm in the $^{1}H,^{15}N$-HSQC spectra of FLNc5 and FLNc4–5 (spectra shown in supplemental Fig. S2). *D,* plot of the chemical shift differences between FLNc5 and FLNc4–5.

Taken together, the crystal structures of FLNa domains 3–5 and FLNc domains 4–5 reveal a new type of Ig-domain packing that fits well with analyses performed in solution stage. The domains 4 and 5 interact relatively tightly, whereas the interface between domains 3 and 4 may be partly flexible.

Ligand Peptide Binds to Domain 4 in the Three Domain Module—Earlier, FLNa domain 4, but not 3 and 5, has been shown to interact with β-strand forming peptides (19). In FLNa3–5 and FLNc4–5 structures, the CD surfaces of all three domains are exposed. However, in domains 3 and 5, the CD loop partially occludes the groove between the β-strands (Fig. 6, *A* and *C*), which is not seen in domain 4. This suggests that only domain 4 may interact via its CD face. However, in FLNc domain 4 but not FLNa, the β-strand C is preceded by a 3_{10} helix (Fig. 6*B*) that might interfere with β-strand augmentation interactions. To test if FLNc domain 4 can still bind a ligand, we co-crystallized the FLNc4–5 fragment with the model peptide derived from GPIb (residues 573–596, RGSLPTFRSSLFLWVRPNGRVGPL), which commonly has the highest interaction affinity among test peptides (19). The structure (Fig. 6*D* and Table 1) revealed that the peptide (residues 577–585) interacts with the typical β sheet augmentation mechanism originally discovered for FLNa domain 17 (11) (Fig. 6, *E* and *F*). Interestingly, the electron density for the 3_{10} helix and the BC loop is not visible in this structure, suggesting local flexibility. We confirmed these interactions in solution by recording ^{15}N- and ^{13}C-HSQC spectra of FLNa3–5 and ^{15}N-HSQC spectra of FLNc4–5 in the presence and absence of the GPIb peptide. Chemical shift perturbations mapped at or close to the CD face of domain 4, indicating that it is available for interaction (Fig. 6, *G* and *H*, and supplemental Fig. S3). This shows that the novel domain-domain interactions between domains 3–5 do not prevent the binding of small β-strand forming peptides to the CD face of domain 4.

Domains 5 Stabilizes the Structure of Domain 4—Isolated domain 4 has been shown to be partially unstable in previous studies (19). To investigate if neighboring domains have an influence on domain 4 stability, we probed the thermal stability of the domains using a hydrophobic fluoroprobe (Fig. 7) (60). Comparison of the temperature-dependent dye binding curves shows that isolated domain 4 starts binding the dye in the range of 35–45 °C, whereas domain 5 binds only in the 70–80 °C range. This indicates that the structure of domain 4 is less stable than domain 5. Furthermore, the dye binding curve of FLNc4–5 shows two transition temperatures. The lower temperature at around 55 °C is considerably higher than that observed with domain 4 alone, whereas the higher transition temperature is close to that of isolated domain 5. This suggests that domain 5 stabilizes domain 4 in the two domain fragment.

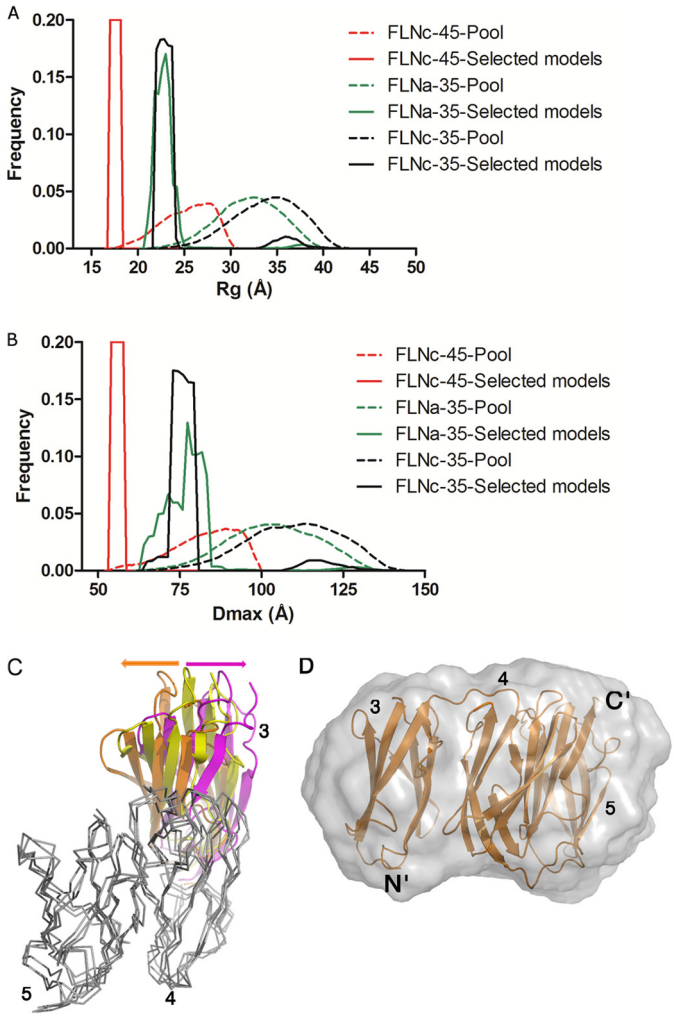

FIGURE 5. **EOM and MD data showing the flexibility of the three-domain fragment.** *A*, R_g and *B*, D_{max} of the pools (*dashed lines*) and the selected models (*solid lines*) for FLNa3–5 (*green*), FLNc3–5 (*black*), and FLNc4–5 (*red*) as internal control. Note that the selected models of FLNc4–5 have a narrow R_g and D_{max} distribution, whereas the selected models of FLNc3–5 and FLNa3–5 show a broader distribution. This suggests that there is more flexibility between domains 3–4 than between domains 4–5. *C*, the superposition of FLNa3–5 crystal structure (domain 3, in *yellow*) with two snapshots from MD simulations (one snapshot with domain 3 in *orange* and the second snapshot with domain 3 in *magenta*). Domains 4 and 5 are shown in *gray* for the crystal structure and MD snapshots and are superimposed using VERTAA module in Bodil (71). The snapshot structures shown represent the most extreme orientations between which domain 3 oscillates during MD simulations. *D*, superposition of one snapshot structure (*orange*) from MD simulations of FLNa3–5 with the SAXS generated *ab initio* envelope (normalized spatial discrepancy of superposition is 2.05).

A similar curve is seen for FLNc3–5 indicating that domain 3 does not have an additional effect on the stability of domain 4.

DISCUSSION

Traditionally, long multidomain proteins are thought to work as beads on a string that allow great flexibility, but where individual domains perform their functions largely independent of each other. This seems not to be the case in FLNs. Although FLNs are flexible molecules composed of 24 similar Ig domains, we have earlier reported three functional domain-domain interactions in the C-terminal rod 2 region of FLNa. In this paper, we tested if there are similar inter-domain interactions in the rod 1 region around domain 4. Our major findings are: 1) domains 3 and 5 interact with domain 4 and this module

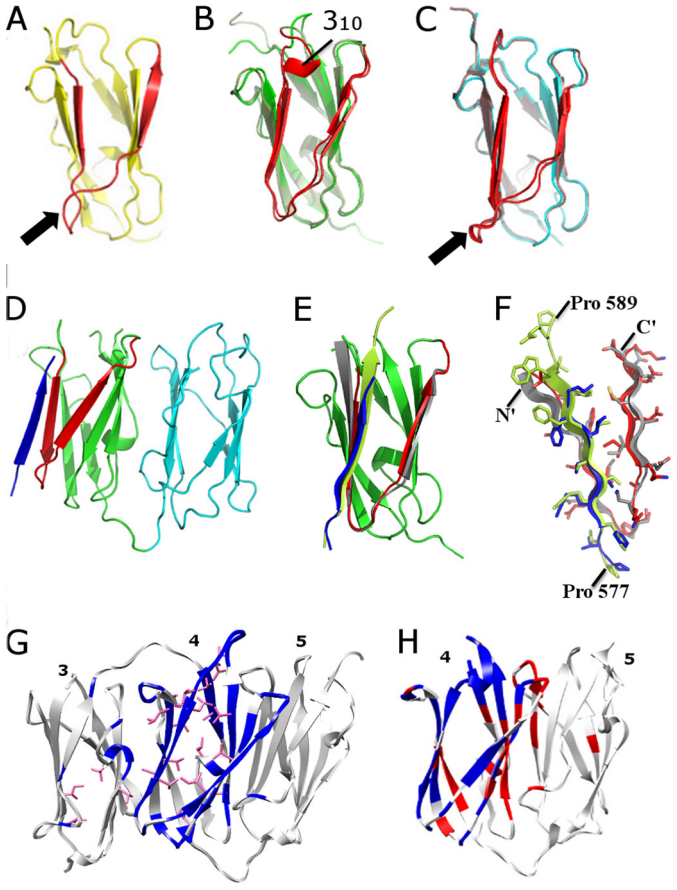

FIGURE 6. **CD face conformation and interactions.** *A–C*, conformation of the CD face of individual domains. In each case, the CD face is shown in *red*. *A*, FLNa3 is shown in *yellow*. *B*, FLNa4 is *green* and FLNc4 is *gray*. Note the 3_{10} helix in FLNc4. *C*, FLNa5 is shown in *cyan* color and FLNc5 is *gray*; closed conformation of the CD loop is marked with an *arrow*. *D*, co-crystal structure of FLNc4–5 with the GPIb peptide (*blue*). *E*, superposition of FLNc4 and GPIb peptide with FLNa17 (*gray*) and GPIb peptide (*lemon*) (root mean square deviation = 0.75 Å between 89 C-α atoms). *F*, detailed view of the peptide conformation with FLNc4 (peptide in *blue*) and FLNa17 (peptide in *lemon*). N and C termini of the CD face of FLNc4 and FLNa17 are labeled. *G*, NMR titration of GPIb with FLNa3–5. Residues undergoing changes in peak intensity and chemical shifts are shown as *blue* (amide group changes) and *pink* side chains (methyl group changes). *H*, residues mapped for the GPIb interaction with FLNc4–5: peaks vanish (*blue*), chemical shift difference more than 0.025 ppm (*red*). $^{1}H,^{15}N$-HSQC spectra for titration of GPIb with FLNa3–5 and FLNc4–5 are shown in supplemental Fig. S3.

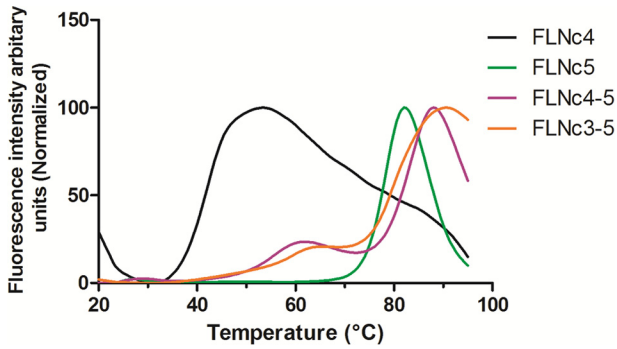

FIGURE 7. **Thermal stability assay showing domain 5 stabilizes domain 4.** Temperature-dependent fluoroprobe binding curves of FLNc4 (*black*), FLNc5 (*green*), FLNc4–5 (*magenta*), and FLNc3–5 (*orange*) are shown.

of FLN domains 3–5 shows a new type of domain-domain arrangement; 2) we show the details of ligand binding to the CD face of FLN domain 4; and 3) provide evidence of domain 4

stabilization by interactions with neighboring domains. We believe that each of these findings has wide implications to our understanding of the FLN function. The findings and their implications are discussed below.

Based on sequence similarity with the pair-forming domains in rod 2 (19, 61), we hypothesized that domain 4 might be involved in domain-domain interactions. To study this, we crystallized FLNa domains 3–5 and FLNc domains 4–5. The structures revealed a novel type of domain packing that has not been observed in Ig domains before. Typically, FLN-type Ig domains interact with each other via the edges of the β sheets and via loop regions (10, 15, 22). On the other hand, many other Ig domains form dimers by interacting perpendicularly face-to-face along their β sheets (62–64). In the current structures, the domains stack on each other and interact face-to-back so that their β sheets are approximately parallel. Because β sheets are rather flat in the FLN-type Ig domains, this kind of arrangement allows maximal interface surface area. This seems to be true particularly between domains 4 and 5, where the interface is governed by several hydrophobic interactions. These features suggest that the interaction between domains 4 and 5 is rather stable. The interface between domains 3 and 4 is slightly shifted, has a smaller area than between 4 and 5, and is mainly polar. These observations suggest that the 3–4 interface may be more flexible than that of 4–5. This was also supported by analysis of SAXS results using EOM and MD simulations. Residues on both interfaces are conserved throughout the animal kingdom and thus it is likely that the arrangement of domains 3–5 observed here is a general feature in FLNs.

To study how domain 4 interacts with the GPIb peptide derived from GPIb, which has been previously shown to interact with FLNa domain 4 and other similar domains (19), we co-crystallized the peptide with FLNc domains 4–5 and used NMR methods to verify the interaction site in solution. The crystal structure showed that interaction of the peptide with FLNc4 is almost identical as with FLNa17 (11): the peptide forms an extra β-strand next to the strand C of domain 4 and interacts hydrophobically with the groove between strands C and D. Using NMR chemical shift perturbation mapping, we were able to show that also in solution the peptide interacts with FLNc4–5 and FLNa3–5 via the CD face of domain 4. This fits well with the observation that in both domains 3 and 5 (FLNa3, FLNa5, and FLNc5), the CD face seems not to be accessible for similar β sheet augmentation interaction because of the CD loop conformation. It is noteworthy that in the unligated FLNc domain 4 there is a 3_{10} helical turn just before strand C that partially occludes the CD groove, but the peptide can induce a conformation change and displace this turn. In the absence of the peptide, NMR spectra revealed two sets of cross-peaks that could be assigned to the residues belonging to the 3_{10} helix, suggesting that this structure has conformational flexibility in a relatively slow ($k_{ex} < 10^3\ s^{-1}$) time scale.[4] This 3_{10} helix is not seen in the structure of FLNa domain 4 and the corresponding residues show only a single set of peaks in ^{15}N-HSQC spectrum. Taken together, these results demonstrate that the CD face of domain 4 is the preferred binding site for β-strand forming peptides within the module of FLN domains 3–5 and that this site is accessible for interactions in this module. Functionally, our findings are in consensus with the hypothesis that there are multiple domains in FLNs to which the same ligand binds (18, 19, 61). In the case of FLNa, this finding is relevant as the interaction between FLNa and GPIb is essential for platelet activation (11, 65). Although mutations in FLNa17 disrupt GPIb interaction in a cell culture model, the highest affinity of GPIb is for FLNa21, and evidence has shown that GPIb binds to multiple sites on FLN (66). It is possible that FLNa17 is the initial binding site for GPIb. This interaction is then complemented by other FLNa domains, including FLNa4. Under force, FLNa21 may then be unmasked and become the strongest binder to facilitate the tight interaction required for platelet adhesion in high shear (67). It is also of interest that the spleen tyrosine kinase, Syk, has been reported to interact with FLNa domain 5 (68). In our current structures the CD faces of FLNa and FLNc domain 5 are occluded by the closed conformation of the CD loop. Thus, the current structures suggest that this interaction of Syk with FLNa domain 5 may use another kind of structural mechanism than β sheet augmentation next to strand C.

In the rod 2 region of FLN the function of domain-domain interactions seems to mask the binding sites on domains 19 and 21. This masking can be relieved by mechanical force and thus these domain-domain interactions provide the basis for the mechanosensor function of FLN (5, 23, 25, 69). In the module of domain 3–5, reported here, we do not see this kind of masking of the known interaction site in domain 4. Thus, CD face masking cannot explain the function of this conserved module. An alternative possibility might be similar to the interaction of FILGAP with domain 23 where mechanical forces on FLN may destabilize interactions (24). It has been observed before that FLNa domain 4 is partially unstructured when studied by NMR (19). Here we show by a hydrophobic fluoroprobe binding assay that domain 5 is required for stabilization of domain 4. Structurally, this can be explained by the hydrophobic surface in domain 4 (particularly the conserved Trp residue at the domain-domain interface), which may cause problems in domain folding when not allowed to interact with domain 5.

In context of diseases, substitution mutations causing familial cardiac valvular dystrophy have been reported in FLNa domain 4 (P637E) and domain 5 (V711D) (70). As this is the first study showing the high resolution structures of these domains, it was of interest to map the location of these residues on our crystal structure of FLNa3–5. We noticed that even though these amino acids were not at the domain-domain interface, the side chains of these residues faced the hydrophobic core made by the β sheets (Fig. 8). Hence, we speculate that mutating the proline or valine to glutamine or aspartate, respectively, will lead to a substantial change in the hydrophobic core and most likely destabilize the individual β sheet domain-fold.

In conclusion, our results highlight that multiple mechanisms have evolved for the inter-domain interactions in FLNs. We report here the presence of a novel three-domain module between domains 3–5 that is conserved in FLNs and partially flexible. We suggest that one function of the three-

[4] Tossavainen, H., Seppälä, J., Sethi, R., Pihlajamaa, T., and Permi, P. (2014) NH, HN, Cα, Cβ, and methyl group assignments of filamin multidomain fragments IgFLNc4–5 and IgFLNa3–5. *Biomol. NMR Assign.* 10.1007/s12104-014-9542-6.

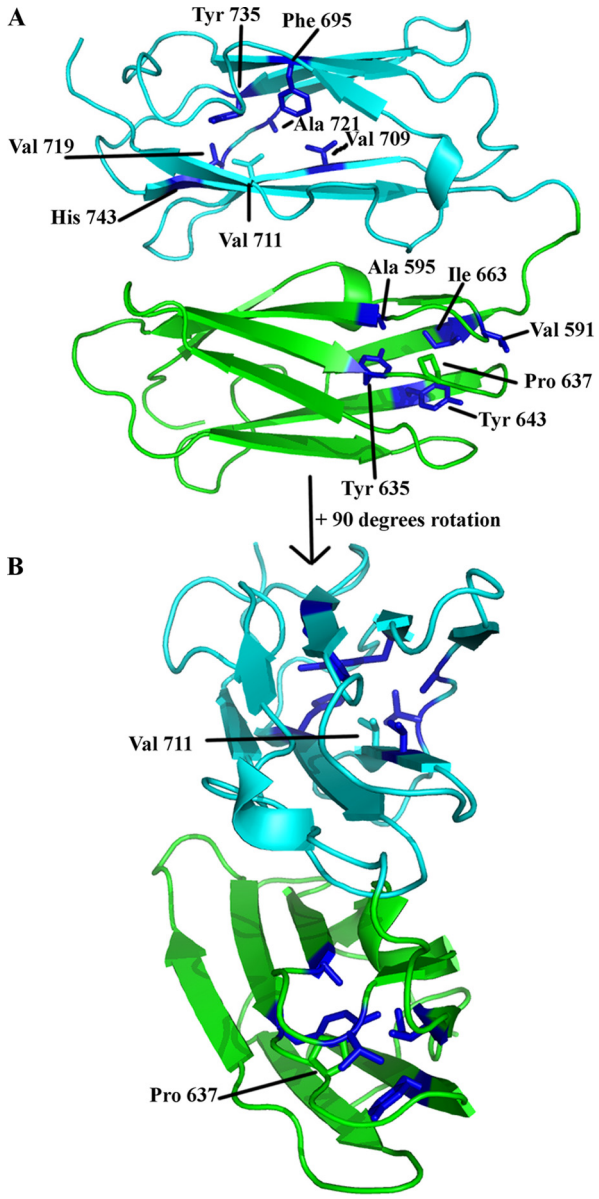

FIGURE 8. **Residues that are mutated in FLNa domains 4 (P637E) and 5 (V711D) causing familial cardiac valvular dystrophy.** *A,* FLNa4 is shown in *green* and FLNa5 in *cyan*. Pro-637 in domain 4 is shown in *green*. The neighboring residues forming the hydrophobic core are shown in *blue*. Val-711 in domain 5 is shown in *cyan*. Neighboring residues forming the hydrophobic core are shown in *blue*. *B,* view rotated by 90 degrees toward the reader.

domain module is to stabilize domain 4 and allow its interactions via the previously characterized β-strand augmentation mechanism.

Acknowledgments—We thank Arja Mansikkaviita for excellent technical assistance. Ulla-Maria Jokipii and Susanna Sinisaari-Kaislo helped in the expression and purification of the proteins. We acknowledge European Molecular Biology Lab (EMBL), European Synchrotron Radiation Facility (ESRF), and MAX-LAB for providing synchrotron access for SAXS and crystal data collection. We express gratitude to Michal J. Gajda (EMBL Hamburg), Matthew Bowler, Adam Round, Petra Pernot (ESRF, Grenoble), Sylvio Haas and Tomás Plivelic (MAX-LAB, Lund) for assistance during data collection at the beamlines. Biocentrum Helsinki and Biocenter Finland are acknowledged for the NMR infrastructure support.

REFERENCES

1. Fürst, D. O., Goldfarb, L. G., Kley, R. A., Vorgerd, M., Olivé, M., and van der Ven, P. F. (2013) Filamin C-related myopathies. Pathology and mechanisms. *Acta Neuropathol.* **125,** 33–46
2. Kley, R. A., Serdaroglu-Oflazer, P., Leber, Y., Odgerel, Z., van der Ven, P. F., Olivé, M., Ferrer, I., Onipe, A., Mihaylov, M., Bilbao, J. M., Lee, H. S., Höhfeld, J., Djinović-Carugo, K., Kong, K., Tegenthoff, M., Peters, S. A., Stenzel, W., Vorgerd, M., Goldfarb, L. G., and Fürst, D. O. (2012) Pathophysiology of protein aggregation and extended phenotyping in filaminopathy. *Brain* **135,** 2642–2660
3. Nakamura, F., Stossel, T. P., and Hartwig, J. H. (2011) The filamins. Organizers of cell structure and function. *Cell Adh. Migr.* **5,** 160–169
4. Nakamura, F., Heikkinen, O., Pentikäinen, O. T., Osborn, T. M., Kasza, K. E., Weitz, D. A., Kupiainen, O., Permi, P., Kilpeläinen, I., Ylänne, J., Hartwig, J. H., and Stossel, T. P. (2009) Molecular basis of filamin A-FilGAP interaction and its impairment in congenital disorders associated with filamin A mutations. *PloS One* **4,** e4928
5. Razinia, Z., Mäkelä, T., Ylänne, J., and Calderwood, D. A. (2012) Filamins in mechanosensing and signaling. *Annu. Rev. Biophys.* **41,** 227–246
6. Zhou, A.-X., Hartwig, J. H., and Akyürek, L. M. (2010) Filamins in cell signaling, transcription and organ development. *Trends Cell Biol.* **20,** 113–123
7. van der Flier, A., and Sonnenberg, A. (2001) Structural and functional aspects of filamins. *Biochim. Biophys. Acta* **1538,** 99–117
8. Stossel, T. P., Condeelis, J., Cooley, L., Hartwig, J. H., Noegel, A., Schleicher, M., and Shapiro, S. S. (2001) Filamins as integrators of cell mechanics and signalling. *Nat. Rev. Mol. Cell Biol.* **2,** 138–145
9. Gorlin, J. B., Yamin, R., Egan, S., Stewart, M., Stossel, T. P., Kwiatkowski, D. J., and Hartwig, J. H. (1990) Human endothelial actin-binding protein (ABP-280, nonmuscle filamin). A molecular leaf spring. *J. Cell Biol.* **111,** 1089–1105
10. Ruskamo, S., and Ylänne, J. (2009) Structure of the human filamin A actin-binding domain. *Acta Crystallogr. D Biol. Crystallogr.* **65,** 1217–1221
11. Nakamura, F., Pudas, R., Heikkinen, O., Permi, P., Kilpeläinen, I., Munday, A. D., Hartwig, J. H., Stossel, T. P., and Ylänne, J. (2006) The structure of the GPIb-filamin A complex. *Blood* **107,** 1925–1932
12. Kiema, T., Lad, Y., Jiang, P., Oxley, C. L., Baldassarre, M., Wegener, K. L., Campbell, I. D., Ylänne, J., and Calderwood, D. A. (2006) The molecular basis of filamin binding to integrins and competition with talin. *Mol. Cell* **21,** 337–347
13. Lad, Y., Jiang, P., Ruskamo, S., Harburger, D. S., Ylänne, J., Campbell, I. D., and Calderwood, D. A. (2008) Structural basis of the migfilin-filamin interaction and competition with integrin tails. *J. Biol. Chem.* **283,** 35154–35163
14. Ithychanda, S. S., Das, M., Ma, Y.-Q., Ding, K., Wang, X., Gupta, S., Wu, C., Plow, E. F., and Qin, J. (2009) Migfilin, a molecular switch in regulation of integrin activation. *J. Biol. Chem.* **284,** 4713–4722
15. Heikkinen, O. K., Ruskamo, S., Konarev, P. V., Svergun, D. I., Iivanainen, T., Heikkinen, S. M., Permi, P., Koskela, H., Kilpeläinen, I., and Ylänne, J. (2009) Atomic structures of two novel immunoglobulin-like domain pairs in the actin cross-linking protein filamin. *J. Biol. Chem.* **284,** 25450–25458
16. Takala, H., Nurminen, E., Nurmi, S. M., Aatonen, M., Strandin, T., Takatalo, M., Kiema, T., Gahmberg, C. G., Ylänne, J., and Fagerholm, S. C. (2008) β2 Integrin phosphorylation on Thr758 acts as a molecular switch to regulate 14-3-3 and filamin binding. *Blood* **112,** 1853–1862
17. Smith, L., Page, R. C., Xu, Z., Kohli, E., Litman, P., Nix, J. C., Ithychanda, S. S., Liu, J., Qin, J., Misra, S., and Liedtke, C. M. (2010) Biochemical basis of the interaction between cystic fibrosis transmembrane conductance regulator and immunoglobulin-like repeats of filamin. *J. Biol. Chem.* **285,** 17166–17176
18. Playford, M. P., Nurminen, E., Pentikäinen, O. T., Milgram, S. L., Hartwig, J. H., Stossel, T. P., and Nakamura, F. (2010) Cystic fibrosis transmembrane conductance regulator interacts with multiple immunoglobulin domains of filamin A. *J. Biol. Chem.* **285,** 17156–17165
19. Ithychanda, S. S., Hsu, D., Li, H., Yan, L., Liu, D. D., Liu, D., Das, M., Plow, E. F., and Qin, J. (2009) Identification and characterization of multiple similar ligand-binding repeats in filamin. Implication on filamin-mediated

receptor clustering and cross-talk. *J. Biol. Chem.* **284,** 35113–35121
20. Pudas, R., Kiema, T.-R., Butler, P. J., Stewart, M., and Ylänne, J. (2005) Structural basis for vertebrate filamin dimerization. *Structure* **13,** 111–119
21. Seo, M.-D., Seok, S.-H., Im, H., Kwon, A.-R., Lee, S. J., Kim, H.-R., Cho, Y., Park, D., and Lee, B.-J. (2009) Crystal structure of the dimerization domain of human filamin A. *Proteins* **75,** 258–263
22. Lad, Y., Kiema, T., Jiang, P., Pentikäinen, O. T., Coles, C. H., Campbell, I. D., Calderwood, D. A., and Ylänne, J. (2007) Structure of three tandem filamin domains reveals auto-inhibition of ligand binding. *EMBO J.* **26,** 3993–4004
23. Pentikäinen, U., and Ylänne, J. (2009) The regulation mechanism for the auto-inhibition of binding of human filamin A to integrin. *J. Mol. Biol.* **393,** 644–657
24. Ehrlicher, A. J., Nakamura, F., Hartwig, J. H., Weitz, D. A., and Stossel, T. P. (2011) Mechanical strain in actin networks regulates FilGAP and integrin binding to filamin A. *Nature* **478,** 260–263
25. Rognoni, L., Stigler, J., Pelz, B., Ylänne, J., and Rief, M. (2012) Dynamic force sensing of filamin revealed in single-molecule experiments. *Proc. Natl. Acad. Sci. U.S.A.* **109,** 19679–19684
26. Ithychanda, S. S., and Qin, J. (2011) Evidence for multisite ligand binding and stretching of filamin by integrin and migfilin. *Biochemistry* **50,** 4229–4231
27. Ruskamo, S., Gilbert, R., Hofmann, G., Jiang, P., Campbell, I. D., Ylänne, J., and Pentikäinen, U. (2012) The C-terminal rod 2 fragment of filamin A forms a compact structure that can be extended. *Biochem. J.* **446,** 261–269
28. Gileadi, O., Burgess-Brown, N. A., Colebrook, S. M., Berridge, G., Savitsky, P., Smee, C. E., Loppnau, P., Johansson, C., Salah, E., and Pantic, N. H. (2008) High throughput production of recombinant human proteins for crystallography. *Methods Mol. Biol.* **426,** 221–246
29. Kabsch, W. (2010) XDS. *Acta Crystallogr. D Biol. Crystallogr.* **66,** 125–132
30. McCoy, A. J., Grosse-Kunstleve, R. W., Adams, P. D., Winn, M. D., Storoni, L. C., and Read, R. J. (2007) Phaser crystallographic software. *J. Appl. Crystallogr.* **40,** 658–674
31. Murshudov, G. N., Vagin, A. A., and Dodson, E. J. (1997) Refinement of macromolecular structures by the maximum-likelihood method. *Acta Crystallogr. D Biol. Crystallogr.* **53,** 240–255
32. Winn, M. D., Ballard, C. C., Cowtan, K. D., Dodson, E. J., Emsley, P., Evans, P. R., Keegan, R. M., Krissinel, E. B., Leslie, A. G., McCoy, A., McNicholas, S. J., Murshudov, G. N., Pannu, N. S., Potterton, E. A., Powell, H. R., Read, R. J., Vagin, A., and Wilson, K. S. (2011) Overview of the CCP4 suite and current developments. *Acta Crystallogr. D Biol. Crystallogr.* **67,** 235–242
33. Emsley, P., and Cowtan, K. (2004) Coot. Model-building tools for molecular graphics. *Acta Crystallogr. D Biol. Crystallogr.* **60,** 2126–2132
34. Langer, G., Cohen, S. X., Lamzin, V. S., and Perrakis, A. (2008) Automated macromolecular model building for x-ray crystallography using ARP/wARP version 7. *Nat. Protoc.* **3,** 1171–1179
35. Krissinel, E., and Henrick, K. (2007) Inference of macromolecular assemblies from crystalline state. *J. Mol. Biol.* **372,** 774–797
36. Pettersen, E. F., Goddard, T. D., Huang, C. C., Couch, G. S., Greenblatt, D. M., Meng, E. C., and Ferrin, T. E. (2004) UCSF Chimera. A visualization system for exploratory research and analysis. *J Comput. Chem.* **25,** 1605–1612
37. Sievers, F., Wilm, A., Dineen, D., Gibson, T. J., Karplus, K., Li, W., Lopez, R., McWilliam, H., Remmert, M., Söding, J., Thompson, J. D., and Higgins, D. G. (2011) Fast, scalable generation of high-quality protein multiple sequence alignments using Clustal Omega. *Mol. Syst. Biol.* **7,** 539
38. Roessle, M. W., Klaering, R., Ristau, U., Robrahn, B., Jahn, D., Gehrmann, T., Konarev, P., Round, A., Fiedler, S., Hermes, C., and Svergun, D. (2007) Upgrade of the small-angle X-ray scattering beamline X33 at the European Molecular Biology Laboratory, Hamburg. *J. Appl. Crystallogr.* **40,** s190–s194
39. Labrador, A., Cerenius, Y., Svensson, C., Theodor, K., and Plivelic, T. (2013) The yellow mini-hutch for SAXS experiments at MAX IV Laboratory. *J. Phys. Conf. Ser.* **425,** 072019
40. Pernot, P., Round, A., Barrett, R., De Maria Antolinos, A., Gobbo, A., Gordon, E., Huet, J., Kieffer, J., Lentini, M., Mattenet, M., Morawe, C., Mueller-Dieckmann, C., Ohlsson, S., Schmid, W., Surr, J., Theveneau, P., Zerrad, L., and McSweeney, S. (2013) Upgraded ESRF BM29 beamline for SAXS on macromolecules in solution. *J. Synchrotron Radiat.* **20,** 660–664
41. Nielsen, S. S., Noergaard Toft, K., Snakenborg, D., Jeppesen, M. G., Jacobsen, J. K., Vestergaard, B., Kutter., J. P., and Arleth, L. (2009). BioXTAS RAW, a software program for highthroughput automated small-angle X-ray scattering data reduction and preliminary analysis. *J. Appl. Crystallogr.* **42,** 959–964
42. Konarev, P. V., Volkov, V. V., Sokolova, A. V., Koch, M. H. J., and Svergun, D. I. (2003). PRIMUS. A Windows PC-based system for small-angle scattering data analysis. *J. Appl. Crystallogr.* **36,** 1277–1282
43. Guinier, A. (1939) La diffraction des rayons X aux très petits angles. Application à l'étude de phénomènes ultramicroscopiques. *Ann. Phys.* **12,** 161–237
44. Svergun, D. I. (1992) Determination of the regularization parameter in indirect-transform methods using perceptual criteria. *J. Appl. Crystallogr.* **25,** 495–503
45. Rambo, R. P., and Tainer, J. A (2011) Characterizing flexible and intrinsically unstructured biological macromolecules by SAS using the Porod-Debye law. *Biopolymers* **95,** 559–571
46. Kratky, O., and Glatter, O. (1982) *Small angle x-ray scattering*, Academic Press, London
47. Franke, D., and Svergun, D. I. (2009) DAMMIF, a program for rapid *ab-initio* shape determination in small-angle scattering. *J. Appl. Crystallogr.* **42,** 342–346
48. Svergun, D. I., Petoukhov, M. V., and Koch, M. H. (2001) Determination of domain structure of proteins from x-ray solution scattering. *Biophys. J.* **80,** 2946–2953
49. Volkov, V. V., and Svergun, D. I. (2003) Uniqueness of *ab initio* shape determination in small-angle scattering. *J. Appl. Crystallogr.* **36,** 860–864
50. Svergun, D., Barberato, C., and Koch, M. H. J. (1995) CRYSOL. A program to evaluate x-ray solution scattering of biological macromolecules from atomic coordinates. *J. Appl. Crystallogr.* **28,** 768–773
51. Bernadó, P., Mylonas, E., Petoukhov, M. V., Blackledge, M., and Svergun, D. I. (2007) Structural characterization of flexible proteins using small-angle x-ray scattering. *J. Am. Chem. Soc.* **129,** 5656–5664
52. Schneider, C. A., Rasband, W. S., and Eliceiri, K. W. (2012) NIH Image to ImageJ. 25 years of image analysis. *Nat. Methods* **9,** 671–675
53. Wang, J., Wang, W., Kollman, P. A., and Case, D. A. (2006) Automatic atom type and bond type perception in molecular mechanical calculations. *J. Mol. Graph. Model.* **25,** 247–260
54. Phillips, J. C., Braun, R., Wang, W., Gumbart, J., Tajkhorshid, E., Villa, E., Chipot, C., Skeel, R. D., Kalé, L., and Schulten, K. (2005) Scalable molecular dynamics with NAMD. *J. Comput. Chem.* **26,** 1781–1802
55. Duan, Y., Wu, C., Chowdhury, S., Lee, M. C., Xiong, G., Zhang, W., Yang, R., Cieplak, P., Luo, R., Lee, T., Caldwell, J., Wang, J., and Kollman, P. (2003) A point-charge force field for molecular mechanics simulations of proteins based on condensed-phase quantum mechanical calculations. *J. Comput. Chem.* **24,** 1999–2012
56. Feller, S. E., Zhang, Y. H., Pastor, R. W., and Brooks, B. R. (1995) Constant pressure molecular dynamics simulation. The Langevin piston method. *J. Chem. Phys.* **103,** 4613–4621
57. Schlick, T., Skeel, R., Brunger, A. T. D., Kale, L. V., Board, J. A. Jr., Hermans, J., and Schulte, K. (1999) Algorithmic challenges in computational molecular biophysics. *J. Comput. Phys.* **151,** 9–48
58. Darden, T., York, D., and Pedersen, L. (1993) Partiicle mesh Ewald-an N Log(N) method for Ewald sums in large systems. *J. Chem. Phys.* **98,** 10089–10092
59. Ryckaert, J. P., Ciccotti, G., and Berendsen, H. J. (1977) Numerical integration of the Cartesian equations of motion of a system with constraints. Molecular dynamics of *n*-alkanes. *J. Comput. Phys.* **23,** 327–341
60. Pantoliano, M. W., Petrella, E. C., Kwasnoski, J. D., Lobanov, V. S., Myslik, J., Graf, E., Carver, T., Asel, E., Springer, B. A., Lane, P., and Salemme, F. R. (2001) High-density miniaturized thermal shift assays as a general strategy for drug discovery. *J. Biomol. Screen.* **6,** 429–440
61. Light, S., Sagit, R., Ithychanda, S. S., Qin, J., and Elofsson, A. (2012) The evolution of filamin. A protein domain repeat perspective. *J. Struct. Biol.* **179,** 289–298
62. Wurzburg, B. A., and Jardetzky, T. S. (2009) Conformational flexibility in

immunoglobulin E-Fc 3–4 revealed in multiple crystal forms. *J. Mol. Biol.* **393,** 176–190
63. Müller, R., Gräwert, M. A., Kern, T., Madl, T., Peschek, J., Sattler, M., Groll, M., and Buchner, J. (2013) High-resolution structures of the IgM Fc domains reveal principles of its hexamer formation. *Proc. Natl. Acad. Sci. U.S.A.* **110,** 10183–10188
64. Biersmith, B. H., Hammel, M., Geisbrecht, E. R., and Bouyain, S. (2011) The immunoglobulin-like domains 1 and 2 of the protein-tyrosine phosphatase LAR adopt an unusual horseshoe-like conformation. *J. Mol. Biol.* **408,** 616–627
65. Feng, S., Reséndiz, J. C., Lu, X., and Kroll, M. H. (2003) Filamin A binding to the cytoplasmic tail of glycoprotein Ibα regulates von Willebrand factor-induced platelet activation. *Blood* **102,** 2122–2129
66. Meyer, S. C., Zuerbig, S., Cunningham, C. C., Hartwig, J. H., Bissell, T., Gardner, K., and Fox, J. E. (1997) Identification of the region in actin-binding protein that binds to the cytoplasmic domain of glycoprotein IBα. *J. Biol. Chem.* **272,** 2914–2919
67. Williamson, D., Pikovski, I., Cranmer, S. L., Mangin, P., Mistry, N., Domagala, T., Chehab, S., Lanza, F., Salem and H. H., Jackson, S. P. (2002) Interaction between platelet glycoprotein Ibα and filamin-1 is essential for glycoprotein Ib/IX receptor anchorage at high shear. *J. Biol. Chem.* **277,** 2151–2159
68. Falet, H., Pollitt, A. Y., Begonja, A. J., Weber, S. E., Duerschmied, D., Wagner, D. D., Watson, S. P., and Hartwig, J. H. (2010) A novel interaction between FlnA and Syk regulates platelet ITAM-mediated receptor signaling and function. *J. Exp. Med.* **207,** 1967–1979
69. Chen, H., Chandrasekar, S., Sheetz, M. P., Stossel, T. P., Nakamura, F., and Yan, J. (2013) Mechanical perturbation of filamin A immunoglobulin repeats 20–21 reveals potential non-equilibrium mechanochemical partner binding function. *Sci. Rep.* **3,** 1642
70. Kyndt, F., Gueffet, J.-P., Probst, V., Jaafar, P., Legendre, A., Le Bouffant, F., Toquet, C., Roy, E., McGregor, L., Lynch, S. A., Newbury-Ecob, R., Tran, V., Young, I., Trochu, J. N., Le Marec, H., Schott, J. J. (2007) Mutations in the gene encoding filamin A as a cause for familial cardiac valvular dystrophy. *Circulation* **115,** 40–49
71. Lehtonen, J. V., Still, D.-J., Rantanen, V.-V., Ekholm, J., Björklund, D., Iftikhar, Z., Huhtala, M., Repo, S., Jussila, A., Jaakkola, J., Pentikäinen, O., Nyrönen, T., Salminen, T., Gyllenberg, M., and Johnson, M. S. (2004) BODIL. A molecular modeling environment for structure-function analysis and drug design. *J. Comput. Aided Mol. Des.* **18,** 401–419